processes

MDPI

Article

Optimal Placement and Sizing of Reactive Power Compensation Devices in Power Grids with High Penetration of Distributed Generation

Nan Feng [1], Tao Niu [2,*], Jun Yan [1], Yufan Zhang [1], Yuyao Feng [1] and Yuli Lei [2]

[1] Electric Power Research Institute, State Grid Shanghai Municipal Electric Power Company, Shanghai 200437, China; powersystem_res@163.com (N.F.); zhangyufan@163.com (Y.Z.); voltage_sh@163.com (Y.F.)
[2] School of Electrical Engineering, Chongqing University, Chongqing 400044, China; yulilei@foxmail.com
* Correspondence: niutthu@cqu.edu.cn; Tel.: +86-17320424266

Abstract

To address voltage stability challenges in power grids with high penetration of distributed generation (DG), this paper proposes an optimal configuration method for reactive power compensation devices. Voltage-weak nodes are first identified using a novel short-circuit ratio (SCR) index. An average electrical distance metric is then introduced to determine optimal installation nodes by computing distances between candidate nodes and weak nodes. Subject to constraints on maximum compensation capacity and allowable DG disconnection limits, MATLAB simulations validate the optimal configuration. Case studies on modified IEEE 9, 14 and 39 bus systems confirm the method's efficacy: DG tripping due to low-/high-voltage ride-through failures is effectively mitigated, with minimum fault voltage increasing by 0.05–0.08 p.u. and voltage recovery time reduced by 0.15–0.8 s.

Keywords: distributed generation; optimal configuration; reactive power compensation device

check for updates

Academic Editor: Hsin-Jang Shieh

Received: 15 August 2025
Revised: 4 September 2025
Accepted: 12 September 2025
Published: 16 September 2025

Citation: Feng, N.; Niu, T.; Yan, J.; Zhang, Y.; Feng, Y.; Lei, Y. Optimal Placement and Sizing of Reactive Power Compensation Devices in Power Grids with High Penetration of Distributed Generation. *Processes* **2025**, *13*, 2953. https://doi.org/10.3390/pr13092953

Copyright: © 2025 by the authors. Licensee MDPI, Basel, Switzerland. This article is an open access article distributed under the terms and conditions of the Creative Commons Attribution (CC BY) license (https://creativecommons.org/licenses/by/4.0/).

1. Introduction

As a significant form of new energy generation, distributed generation holds broad development prospects [1,2]. Sustained socio-economic growth necessitates the accelerated construction of robust smart grids. Taking distributed photovoltaic (PV) generation as an example, China's cumulative installed capacity of distributed PV reached 157.6 GW by the end of 2022, accounting for 40.2% of the total PV installed capacity, with distributed PV contributing 58.5% of the newly grid-connected PV capacity in 2022 [3,4].

The large-scale integration of distributed generation alters the voltage stability characteristics of power grids [5]. DG systems typically connect at low voltage levels to structurally weak points in the system [6]. During severe grid faults, significant voltage fluctuations at DG connection points can cause low-voltage or high-voltage ride-through failures and subsequent disconnection, jeopardizing the secure and stable operation of the grid [7,8]. Large-scale DG integration induces bidirectional power flow and reduces system inertia, causing voltage deviations. This triggers failures during N-1 faults, leading to DG disconnections that compromise grid security. DG integration challenges traditional grid operation modes and stability, particularly regarding voltage stability. Characteristics such as intermittent and stochastic power output from DG systems can induce voltage fluctuations, deviations, and even local voltage imbalances. These issues not only compromise grid security but also adversely affect power supply quality for end-users [9].

Therefore, optimizing the configuration of reactive power compensation devices in grids with large-scale DG integration is urgently needed to provide reactive power and voltage support, thus ensuring secure and stable grid operation.

Consequently, reactive power compensation for grids with large-scale DG systems is imperative. Reactive compensation devices fall into two main categories: series compensation and shunt compensation. Series compensation, commonly used in Europe and the US, enhances line transmission capacity by controlling impedance parameters. By contrast, shunt compensation predominates in China for voltage control. Shunt compensation is further divided into system compensation and load compensation. System compensation improves stability, enhances transmission capacity, reduces losses, and optimizes reactive power flow, and it is typically applied to AC transmission/distribution systems. Load compensation improves voltage quality and power factor, targeting end-user loads. Load compensation includes static and dynamic methods.

Static compensation employs capacitor/reactor banks at load points to balance three-phase loads. While structurally simple, cost-effective, and beneficial for static stability, its reactive power output decreases during voltage sags, potentially worsening system voltage during transient instability. Transient voltage instability primarily stems from localized reactive power shortages during rapid load increases or high proportions of induction motor loads [10]. Thus, even with sufficient static reactive reserves, systems may face voltage collapse risks following faults or operations. For large receiving-end systems, static compensation alone is inadequate for meeting operational security requirements.

Current research extensively investigates voltage characteristics and reactive power configurations after integrating traditional renewable energy plants. Existing static reactive optimization primarily targets synchronous grids, aiming to reduce losses, improve voltage profiles, enhance stability, and lower costs. Reactive compensation device configuration becomes critical for ensuring stable system operation [10]. References [11,12] addresses challenges in traditional reactive power optimization methods—long computation times and uncertain convergence under large-scale DG integration. It proposes a generalized master–slave splitting algorithm considering transient voltage security constraints for collaborative optimization. References [13,14] highlight that transient over-voltage issues in sending-end systems caused by AC/DC faults restrict HVDC transmission limits and hinder renewable energy absorption. Reference [15] presents a dynamic reactive power planning method using trajectory sensitivity and singular value decomposition for site selection and capacity optimization. Reference [16] introduces a transient voltage stability index to guide compensation device placement via compensation sensitivity. However, research on reactive optimization post-large-scale DG integration remains limited, necessitating deeper study incorporating DG disconnection behaviors under various faults. Unlike traditional grids, distributed generation poses two key challenges: (1) output depends on uncontrollable natural conditions, exhibiting unpredictability and instability; and (2) grid connection relies on power electronic converters, which lack mechanical inertia and involve complex, multi-timescale control logic, introducing operational challenges [17,18]. Existing studies focus on centralized renewables or ignore DG disconnection behaviors. Critical gaps remain: (1) heuristic device placement lacks electrical distance metrics; and (2) static compensation fails transient stability.

This paper proposes an optimal configuration method for reactive power compensation devices addressing voltage stability issues post-large-scale DG integration. First, voltage-weak nodes are identified using the SCR index. An average electrical distance metric is then introduced. Compensation device installation nodes are determined by calculating between candidate nodes and weak nodes. Finally, under constraints of maximum compensation capacity and allowable DG disconnection, the optimal configuration is de-

rived via MATLAB R2023b simulations. Testing on modified IEEE 9, 14 and 39 bus systems validates the method's feasibility. Our work bridges these gaps through three innovations: (1) an SCR < 2.0 threshold for weak node identification, validated on IEEE systems; (2) an average electrical distance metric replacing heuristic placement; (3) chance-constrained programming integrating DG disconnection limits with confidence level.

2. Short-Circuit Ratio Index

The short-circuit ratio (SCR) measures the relative strength of the AC system in supporting converter bus voltage during faults. A higher SCR indicates stronger support and a lower risk of commutation failures [19]. First, DG partitions $i(i = 1, 2, \ldots m)$ are defined based on current and projected developments. The New Energy SCR is calculated for each DG to identify weak nodes:

$$SCR_i = \frac{S_{SC_i}}{P_{dN_i}} \tag{1}$$

where SCR_i is the ratio of short-circuit capacity; S_{SCi} is the short-circuit capacity of nodes i distributed power sources and P_{dNi} is the rated capacity of nodes i distributed power sources. Nodes with $SCR_i < 2$ are deemed weak and recorded in set $\boldsymbol{R} = \{i, j, \ldots\}$.

2.1. Multi-Infeed HVDC Systems

For systems with multiple HVDC infeed points concentrated in one receiving-end grid, as in Figure 1, single-infeed SCR calculations fail to account for interactions between DC systems, yielding overly optimistic results. The Multi-Infeed Short-Circuit Ratio (MISCR) incorporates these interactions [20]:

$$MISCR_j = \frac{S_{sci}}{P_{deqi}} = \frac{|U_{si} I_{sci}|}{P_{dNi} + \sum\limits_{j,j\neq i} (MIIF_{ji} \times P_{dNj})} \tag{2}$$

where S_{sci} is the short-circuit capacity at node i (product of rated voltage U_{si} and three-phase short-circuit current I_{Sci}). P_{deqi} is the equivalent DC rated power at node i. P_{dNi} and P_{dNj} are the rated powers of inverter stations at nodes i and j, respectively. $MIIF_{ji}$ is the Multi-Infeed Interaction Factor.

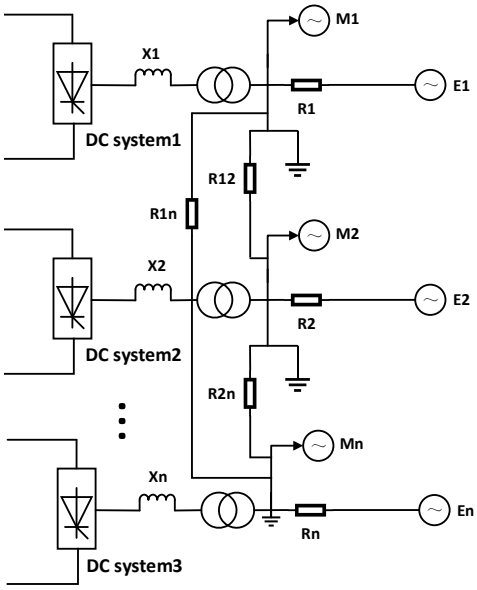


Figure 1. Multi-DC centralized feed system.

The $MIIF_{ji}$ between nodes i and j is defined as the ratio of voltage change at node $j(\Delta U_j)$ to that at node $i(\Delta U_i)$ during a symmetrical inductive ground fault or reactor switching causing a 1% voltage drop at node i under rated conditions [21]:

$$MIIF_{ji} = \frac{\Delta U_j}{\Delta U_i} = \frac{\Delta U_j}{1\% U_{i0}} \tag{3}$$

where U_{i0} is the pre-fault voltage at node i; ΔU_j, ΔU_i and U_{i0} are per-unit values.

2.2. Multiple Renewable Plants Systems

For systems with multiple renewable (wind/PV) plants connected to the same grid, as in Figure 2, the traditional SCR is insufficient. The Equivalent Short-Circuit Ratio (ESCR) evaluates the electrical strength of multi-converter systems. A low ESCR indicates a weak system with high instability risk.

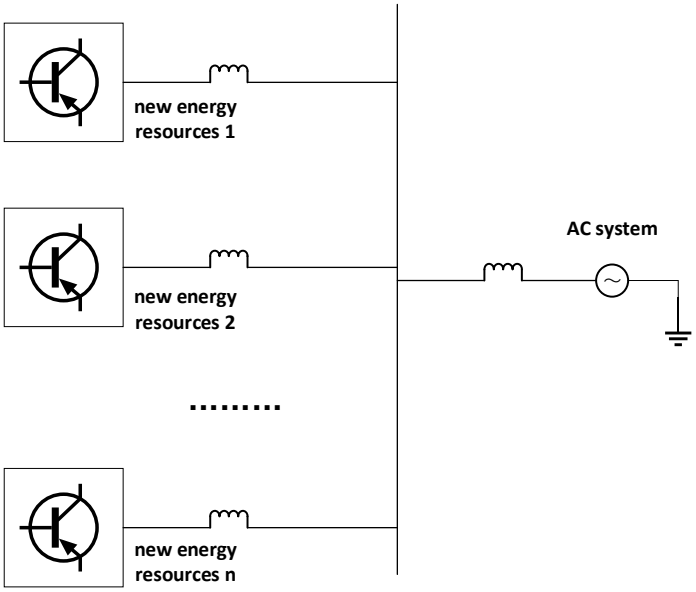


Figure 2. Wind power grid connected system.

ESCR calculation is based on the observation of voltage disturbances. The Wind/PV Interaction Factor (WPIF) quantifies voltage changes at node i caused by perturbations at node j [22]:

$$WPIF_{ij} = \frac{\Delta v_i}{\Delta v_j} \tag{4}$$

where Δv_i is the voltage change at node i induced by a voltage fluctuation Δv_j at node j. WPIF approaches 0 for distant nodes and 1 for closely coupled nodes.

When multiple wind/PV plants connect to the same AC grid with close electrical proximity, the short-circuit capacity at grid interconnection points is significantly lower than at collector buses. Considering adjacent plant influences, the ESCR is defined as follows [22]:

$$ESCR = \frac{S_i}{P_{WFi} + \sum_j \left(WPIF_{ji} \times P_{WFi}\right)} \tag{5}$$

where S_i is the short-circuit capacity at the point of interconnection i, P_{WFi} is the active power output of the wind/PV plant at i and $\sum(WPIF_{ji} \times PWF_j)$ represents the cumulative impact of adjacent plants.

3. Selection of Installation Nodes for Reactive Compensation Devices

Compensation effectiveness generally improves with shorter electrical distance to reactors. Therefore, the optimal installation node should minimize the average electrical distance to all weak nodes. First, the node impedance matrix $\boldsymbol{Z}_B$ is formed:

$$Z_B = Y_B^{-1} = \begin{bmatrix} Z_{11} & Z_{12} & \cdots Z_{1n} \\ Z_{21} & Z_{22} & \cdots Z_{2n} \\ \cdots & \cdots & \cdots \\ Z_{n1} & Z_{n2} & \cdots Z_{nn} \end{bmatrix}. \tag{6}$$

where $\mathbf{Y}_\mathrm{B}{}^{-1}$ is the inverse of the nodal admittance matrix. The average electrical distance metric $\mathrm{D_k}$ for candidate node k to weak nodes in set $\boldsymbol{R} = \{i, j, \ldots\}$ is defined as follows:

$$D_k = \frac{\sum\limits_{i \in R} |Z_{kk} + Z_{ii} - 2Z_{ki}|}{num(R)} \tag{7}$$

where $\mathrm{Z_{ki}}$ is the element in row k, column i of $\mathbf{Z}_\mathrm{B}$, and num($\boldsymbol{R}$) is the number of weak nodes. $\mathrm{D_k}$ is computed for all candidate nodes. The node with the smallest $\mathrm{D_k}$ is selected for compensation device installation.

4. Optimization Method for Reactive Compensation Device Configuration

A typical fault set is established based on grid specifics, including critical N-1 and N-2 permanent faults for lines and transformers.

MATLAB simulations analyze optimal installation nodes. Dynamic reactive devices (SVC (GE Renewable Energy, Paris, France), STATCOM (Liaoning Rongxin Xingye Power Technology Co., Ltd, Anshan, China)) are installed at optimal nodes, and variations in total DG disconnection under different faults are assessed. For device k, capacity is increased from 0 to S_{km}. The capacity $S_{N.\max}$, where further increases no longer reduce total DG disconnection under typical faults, is identified as optimal.

Constraints include the maximum allowable DG disconnection $P_{\mathrm{cut.max}}$ and maximum device capacity $S_{N.\max}$ to control costs:

$$P_{cut} \leq P_{cut.\max} \tag{8}$$

$$S_{km} \leq S_{N.\max} \tag{9}$$

The optimization objective function minimizes cost while satisfying constraints:

$$\min F = \lambda P_{cut} + \mu \sum_{j=1}^{N_m} S_j \tag{10}$$

where λ is the penalty coefficient for DG disconnection, and μ is the penalty coefficient for compensation device capacity.

The overall process is shown in Figure 3.

4.1. Chance-Constrained Programming

Chance-constrained programming handles constraints containing random variables, allowing solutions that may violate constraints with low probability while ensuring feasibility above a specified confidence level [23]:

$$\begin{aligned} &\min \overline{f} \\ &\text{s.t.} \begin{cases} \Pr\left\{ f(x,\xi) \le \overline{f} \right\} \ge \beta \\ \Pr\{ g_i(x,\xi) \le 0 \} \ge \alpha \; i = 1,2,\ldots,m \end{cases} \end{aligned} \tag{11}$$

where $f(x,\xi)$ is the objective function, x is the decision vector, ξ is a random vector, $g_i(x,\xi)$ are stochastic constraint functions, $\Pr\{\cdot\}$ denotes probability and α, β are confidence levels. $\overline{f}$ is the minimum value of $f(x,\xi)$ achievable with probability $\ge \beta$.

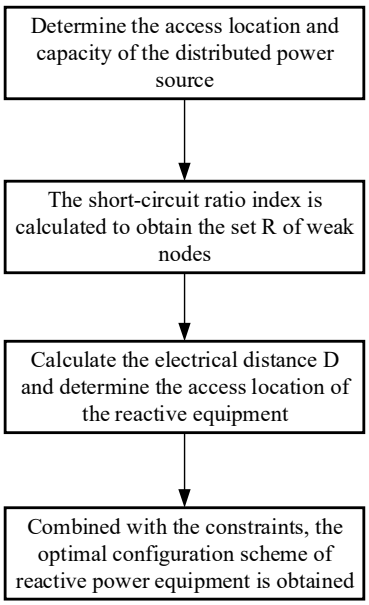


Figure 3. Flow chart of optimal configuration method of reactive power compensation device.

4.2. Constraints

Equality Constraints (Power Flow Equations) are calculated as follows:

$$\begin{cases} P_i^\delta = U_i^\delta \sum\limits_{j \in i} U_j^\delta (G_{ij}^\delta \cos\theta_{ij}^\delta + B_{ij}^\delta \sin\theta_{ij}^\delta) \\ Q_i^\delta = U_i^\delta \sum\limits_{j \in i} U_j^\delta (G_{ij}^\delta \sin\theta_{ij}^\delta - B_{ij}^\delta \cos\theta_{ij}^\delta) \end{cases} \tag{12}$$

where ${P_i}^\delta$, ${Q_i}^\delta$ are active/reactive power injections at node i, respectively; ${U_i}^\delta$, ${U_j}^\delta$ are voltages; ${\theta_{ij}}^\delta$ is the voltage phase difference and ${G_{ij}}^\delta$, ${B_{ij}}^\delta$ are line conductance/susceptance, respectively.

Inequality Constraints (Chance-Constrained) are calculated as follows:

$$\begin{cases} \Pr(U_{i,\min}^\delta \le U_i^\delta \le U_{i,\max}^\delta) \ge \beta_1^\delta \\ \Pr(S_{l,\min}^\delta \le S_l^\delta \le S_{l,\max}^\delta) \ge \beta_2^\delta \end{cases} \tag{13}$$

where $U_{i,\min}^\delta$, $U_{i,\max}^\delta$ are voltage limits; β_1^δ is the voltage confidence level; $S_{l,\min}^\delta$, $S_{l,\max}^\delta$ are line power flow limits and β_2^δ is the line flow confidence level.

Device Output and Capacity Constraints are calculated as follows:

$$\begin{cases} P^{\delta}_{\mathrm{w,min}} \le P^{\delta}_{\mathrm{w}} \le P^{\delta}_{\mathrm{w,max}} \\ Q^{\delta}_{\mathrm{w,min}} \le Q^{\delta}_{\mathrm{w,max}} \le Q^{\delta}_{\mathrm{w,max}} \\ P^{\delta}_{pv,\mathrm{min}} \le P^{\delta}_{pv} \le P^{\delta}_{pv,\mathrm{max}} \\ Q^{\delta}_{pv,\mathrm{min}} \le Q^{\delta}_{pv,\mathrm{max}} \le Q^{\delta}_{pv,\mathrm{max}} \\ Q^{\delta}_{ci,\mathrm{min}} \le Q^{\delta}_{ci} \le Q^{\delta}_{ci,\mathrm{max}} \\ Q^{\delta}_{li,\mathrm{min}} \le Q^{\delta}_{li} \le Q^{\delta}_{li,\mathrm{max}} \end{cases} \tag{14}$$

where $Q^{\delta}_{ci,\mathrm{max}}$ and $Q^{\delta}_{ci,\mathrm{min}}$ represent the upper and lower limits of the capacitor capacity allowed to be installed at node i, respectively; $Q^{\delta}_{li,\mathrm{max}}$ and $Q^{\delta}_{li,\mathrm{min}}$ represent the upper and lower limits of the reactor capacity allowed to be installed at node i, respectively; $P^{\delta}_{\mathrm{w,max}}$ and $P^{\delta}_{\mathrm{w,min}}$ represent the upper and lower limits of the active power output of the wind turbine, respectively; $Q^{\delta}_{\mathrm{w,max}}$ and $Q^{\delta}_{\mathrm{w,min}}$ represent the upper and lower limits of the reactive power output of the wind turbine, respectively; $P^{\delta}_{pv,\mathrm{max}}$ and $P^{\delta}_{pv,\mathrm{min}}$ represent the upper and lower limits of the active power output of the photovoltaic system, respectively, and $Q^{\delta}_{pv,\mathrm{max}}$ and $Q^{\delta}_{pv,\mathrm{min}}$ represent the upper and lower limits of the reactive power output of the photovoltaic system, respectively.

Assuming that node voltages and line flows follow normal distributions, the cumulative distribution functions $Y(U^{\delta}_{i})$, $Y(S^{\delta}_{l})$ obtained via point-estimation methods allow the rewriting of Equation (13) as follows:

$$\begin{cases} Y(U^{\delta}_{i,\mathrm{max}}) - Y(U^{\delta}_{i,\mathrm{min}}) \ge \beta^{\delta}_{1} \\ Y(S^{\delta}_{l,\mathrm{max}}) - Y(S^{\delta}_{l,\mathrm{min}}) \ge \beta^{\delta}_{2} \end{cases} \tag{15}$$

Penalty functions embed constraint violations into the objective:

$$\begin{aligned} &\min F_{\delta} = \\ &\min[f_{\delta} + \lambda_1 \cdot \sum_{i=1}^{M} P(U^{\delta}_{i}) + \lambda_2 \cdot \sum_{l=1}^{n_b} P(S^{\delta}_{l})] \end{aligned} \tag{16}$$

where λ_1, λ_2 are penalty coefficients, and M is node count. Penalty terms are calculated as follows:

$$P(U^{\delta}_{i}) = \begin{cases} \beta^{\delta}_{1} - [Y(U^{\delta}_{i,\mathrm{max}})] & Y(U^{\delta}_{i,\mathrm{max}}) < \beta^{\delta}_{1} \\ 0, & Y(U^{\delta}_{i,\mathrm{max}}) \ge \beta^{\delta}_{1} \end{cases} \tag{17}$$

$$P(S^{\delta}_{l}) = \begin{cases} \beta^{\delta}_{2} - \left[Y\left(S^{\delta}_{l,\mathrm{max}}\right)\right], & Y\left(S^{\delta}_{l,\mathrm{max}}\right) < \beta^{\delta}_{2} \\ 0, & Y\left(S^{\delta}_{l,\mathrm{max}}\right) \ge \beta^{\delta}_{2} \end{cases} \tag{18}$$

4.3. Reactive Power Allocation Capacity

This study employs switchable capacitors as the primary reactive power compensation measure. Considering potential over-voltage conditions during system light-load operations, switchable reactors are concurrently adopted as supplementary compensation devices. The unit compensation capacity of individual capacitor banks and reactor units is predetermined.

The configuration principle for reactive power compensation equipment is established as follows: When the system operates under minimum load conditions, an Optimal Power Flow algorithm is solved. Should the optimal solution yield a negative reactive power compensation value at any node, inductive reactive power compensation must be provided

at that node, with capacity equal to the absolute value of the calculated deficit. Conversely, if the solution yields a positive value, capacitive reactive power compensation should be implemented. This fundamental principle for determining compensation type based on the sign of the OPF-derived reactive power compensation value applies equally under maximum load conditions and normal load conditions.

Given the variation in the required installed compensation capacity across different loading scenarios, the methodology for determining the final system planning scheme and investment cost calculation is specified: Reactive power planning schemes are computed separately for each distinct load level. For each node, the maximum required compensation capacity identified across all load-level analyses is selected as the final planned capacity for that node. This capacity selection approach minimizes the total investment cost for reactive power compensation equipment while ensuring adequate reactive support across all operational scenarios.

5. Case Study Analysis

5.1. System Analysis

To validate the effectiveness of the proposed method, this study employs modified IEEE 9, 14 and 39 bus systems. Selected transmission lines were converted to DC links, and conventional generators were replaced with wind turbines and photovoltaic systems. Pre-selected reactive compensation installation buses were Bus 1, Bus 2 and Bus 3. System configurations are shown in Figures 4–6, with short-circuit ratios (SCR) provided in Tables 1–3.

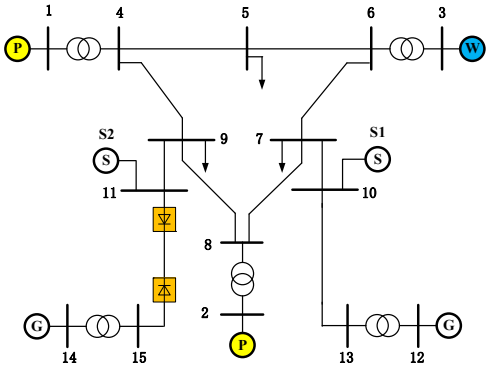


Figure 4. Improved IEEE 9 bus system structure diagram, G stands for generator, W for wind power, P for photovoltaic, S for dynamic compensation equipment, and orange for direct current.

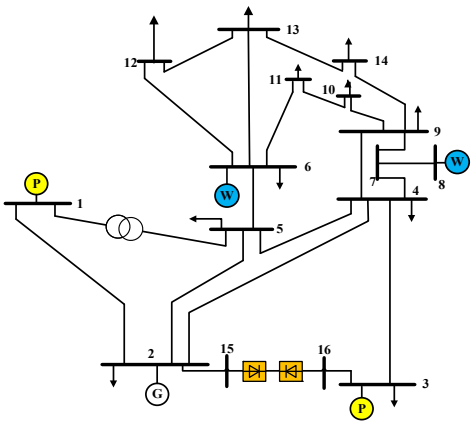


Figure 5. Improved IEEE 14 bus system structure diagram.

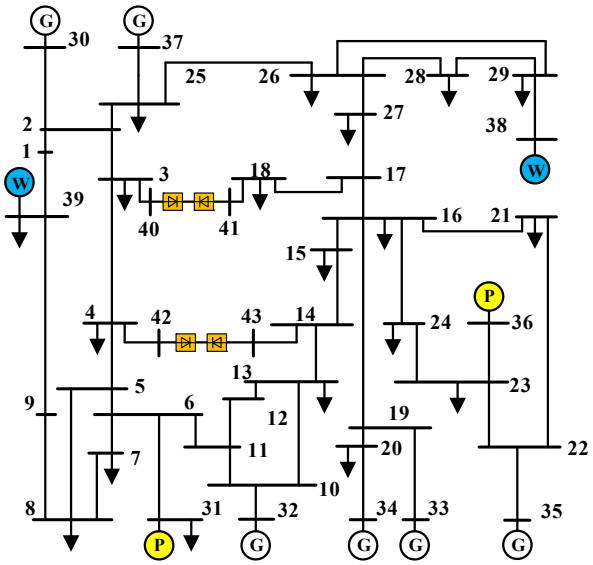


Figure 6. Improved IEEE 39 bus system structure diagram.

Table 1. Improved IEEE 9 bus system circuit ratio.

Bus	SCR	Bus	SCR
Bus 1	2.156	Bus 9	1.785
Bus 2	2.037	Bus 10	2.012
Bus 3	1.456	Bus 11	1.874
Bus 4	2.135	Bus 12	1.984
Bus 5	2.564	Bus 13	2.121
Bus 6	1.795	Bus 14	2.254
Bus 7	2.125	Bus 15	2.214
Bus 8	1.845		

Table 2. Improved IEEE 14 bus system circuit ratio.

Bus	SCR	Bus	SCR
Bus 1	2.178	Bus 9	2.231
Bus 2	2.037	Bus 10	2.090
Bus 3	2.009	Bus 11	2.186
Bus 4	2.184	Bus 12	2.232
Bus 5	2.245	Bus 13	2.091
Bus 6	1.245	Bus 14	2.270
Bus 7	2.066	Bus 15	2.121
Bus 8	1.365	Bus 16	2.200

SCR calculations revealed Bus 3 (SCR = 1.456 < 2.0) as a voltage-weak node. The average electrical distances in the improved IEEE 9 bus system between the candidate compensation buses and the weak node are shown in Table 4.

Table 3. Improved IEEE 39 bus system circuit ratio.

Bus	SCR	Bus	SCR	Bus	SCR
Bus 1	2.178	Bus 16	2.207	Bus 31	2.027
Bus 2	2.037	Bus 17	2.195	Bus 32	2.024
Bus 3	2.009	Bus 18	2.293	Bus 33	2.193
Bus 4	2.184	Bus 19	2.169	Bus 34	2.192
Bus 5	2.245	Bus 20	2.189	Bus 35	2.290
Bus 6	2.006	Bus 21	2.074	Bus 36	2.140
Bus 7	2.066	Bus 22	2.043	Bus 37	2.111
Bus 8	2.063	Bus 23	2.231	Bus 38	1.432
Bus 9	2.219	Bus 24	2.090	Bus 39	1.356
Bus 10	2.056	Bus 25	2.186	Bus 40	2.048
Bus 11	2.126	Bus 26	2.232	Bus 41	1.982
Bus 12	2.132	Bus 27	2.091	Bus 42	2.079
Bus 13	2.298	Bus 28	2.270	Bus 43	2.145
Bus 14	2.236	Bus 29	2.121		
Bus 15	2.122	Bus 30	2.200		

Table 4. Improved IEEE 9 bus system average electrical distance between pre-selected installation positions.

Bus	Initial Value
Bus 1	0.1548
Bus 2	0.1546
Bus 3	0.412

As demonstrated in Tables 1 and 4, Bus 3 is identified as the optimal reactive compensation location for the improved IEEE 9 bus system.

The voltage-weak nodes identified were Bus 6 (SCR = 1.245) and Bus 8 (SCR = 1.365), both below the 2.0 threshold. The average electrical distances in the improved IEEE 14 bus system are shown in Table 5.

Table 5. Improved IEEE 14 bus system average electrical distance between pre-selected installation positions.

Bus	Initial Value
Bus 1	0.1542
Bus 2	0.1246
Bus 3	0.1620

As shown in Tables 2 and 5, Bus 2 is optimal for reactive compensation in the improved IEEE 14 bus system.

The voltage-weak nodes identified were Bus 38 (SCR = 1.432) and Bus 39 (SCR = 1.356). The average electrical distances in the improved IEEE 39 bus system are shown in Table 6.

Table 6. Improved IEEE 39 bus system average electrical distance between pre-selected installation positions.

Bus	Initial Value
Bus 1	0.1330
Bus 2	0.1387
Bus 3	0.2820

As demonstrated in Tables 3 and 6, Bus 1 is optimal for reactive compensation in the improved IEEE 39 bus system.

5.2. Validation Results

Validation was performed using MATLAB (fault duration: 0.1–0.2 s) with 150 Mvar switchable capacitor banks.

After the installation of a 50 Mvar capacitor bank at Bus 3, the voltage response at Bus 6 demonstrated significant improvement. During the fault event, the minimum voltage increased from 0.50 p.u. to 0.55 p.u., while the steady-state voltage rose from 0.95 p.u. to 1.00 p.u. The voltage stabilization time was reduced by approximately 0.8 s. Additionally, voltage fluctuation amplitudes at other buses were correspondingly diminished, resulting in a marked enhancement of the overall voltage stability of the system, as depicted in Figure 7. Comparative analysis of the voltage profiles pre- and post-device optimization reveals that the duration required for Bus 6's voltage to recover to steady-state conditions was substantially shortened. Post-optimization, the voltage stability across all buses improved significantly, as illustrated in Figure 8.

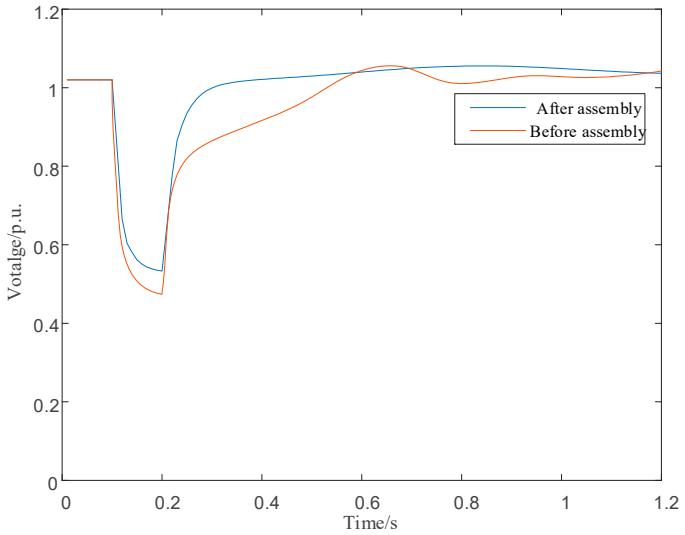


Figure 7. Improved Bus 6 voltage of IEEE 9 bus system.

Following the activation of a 75 Mvar capacitor bank at Bus 2, the voltage profile at Bus 6 demonstrated significant improvement. During the fault event, the minimum voltage increased from 0.50 p.u. to 0.58 p.u., while the voltage stabilization time was reduced by approximately 0.2 s. Additionally, voltage fluctuation amplitudes at other buses were correspondingly diminished, resulting in a marked enhancement of the overall voltage stability of the system, as depicted in Figure 9. Comparative analysis of voltage profiles pre- and post-device optimization reveals that the duration required for Bus 6's voltage to recover to steady-state conditions was substantially shortened. Post-optimization, the voltage stability across all buses improved significantly, as illustrated in Figure 10.

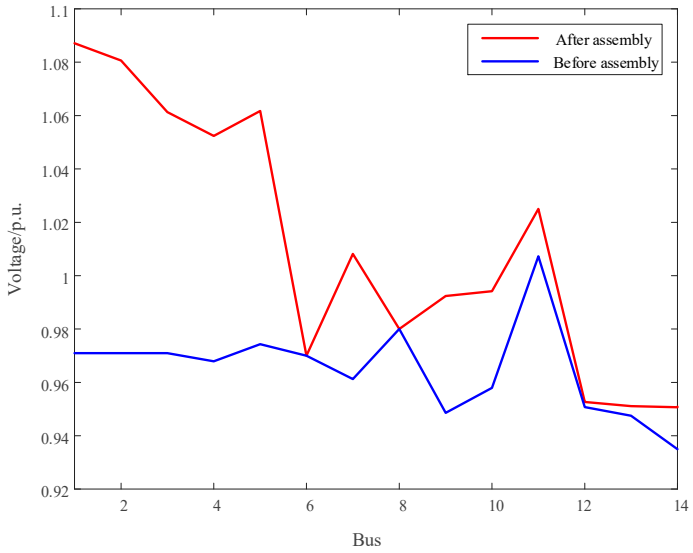


Figure 8. Improved voltage curve comparison of IEEE 9 bus system optimization algorithm.

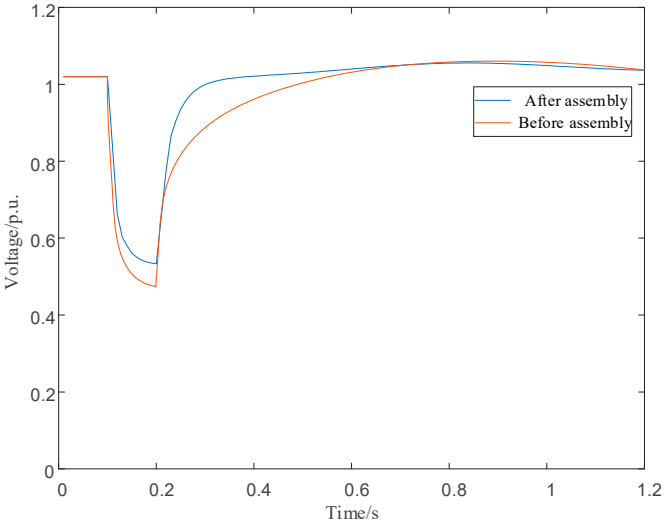


Figure 9. Improved Bus 6 voltage of IEEE 14 bus system.

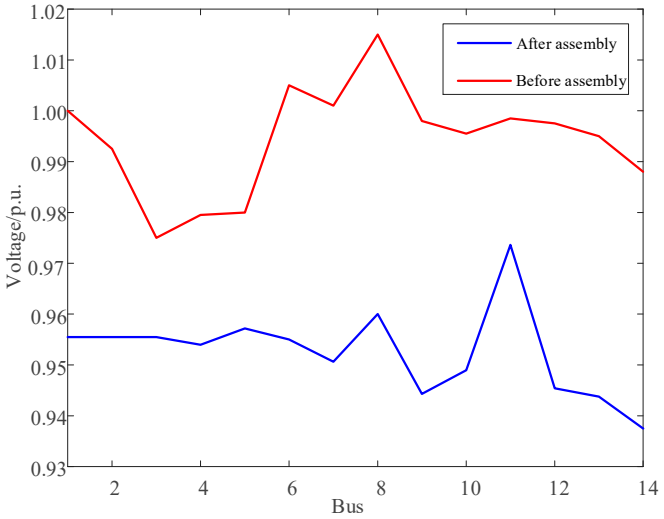


Figure 10. Improved voltage curve comparison of IEEE 14 bus system optimization algorithm.

Following the activation of a 150 Mvar capacitor bank at Bus 1, the voltage profile at Bus 6 demonstrated significant improvement. During the fault event, the minimum voltage increased from 0.50 p.u. to 0.58 p.u., while the voltage stabilization time was reduced by approximately 0.15 s. Additionally, voltage fluctuation amplitudes at other buses were correspondingly diminished, resulting in a marked enhancement of the overall voltage stability of the system, as depicted in Figure 11. Comparative analysis of voltage profiles pre- and post-device optimization reveals that the duration required for Bus 6's voltage to recover to steady-state conditions was substantially shortened. Post-optimization, the voltage stability across all buses improved significantly, as illustrated in Figure 12.

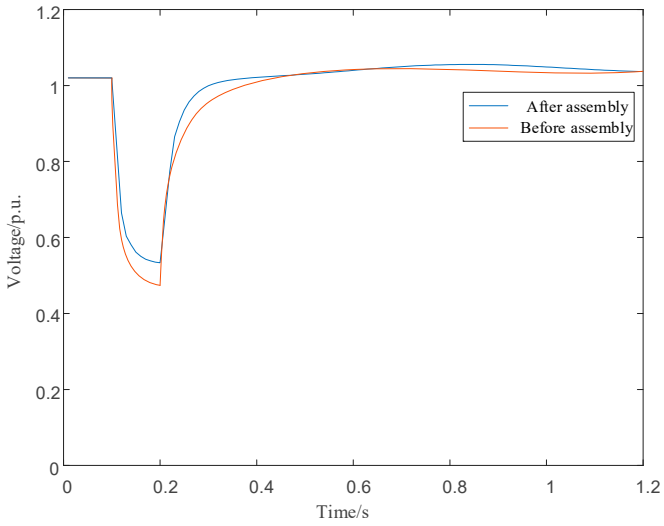


Figure 11. Improved Bus 6 voltage of IEEE 39 bus system.

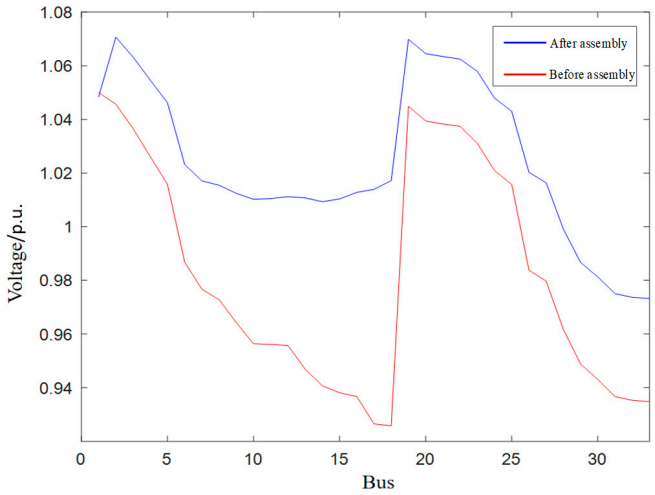


Figure 12. Improved voltage curve comparison of IEEE 39 bus system optimization algorithm.

The practical implications of these voltage improvements are critical for grid compliance and operational resilience. The 0.05–0.08 p.u. increase in minimum fault voltage ensures that voltage nadirs remain safely above the IEEE 1547 LVRT threshold of 0.15 p.u. during severe disturbances, preventing unnecessary DG disconnections. For example, at Bus 6 in the IEEE 9 bus system, as shown in Figure 7, the pre-compensation voltage dipped to 0.50 p.u., risking violation, while the post-compensation voltage was sustained at 0.55 p.u., achieving compliance margins. Simultaneously, the 0.15–0.8 s reduction in voltage recovery time minimizes transient over-voltage and under-voltage durations, reducing protection relay misoperation risks during fault recovery. As demonstrated in the

IEEE 39 bus system, with the results depicted in Figure 11, the voltage stabilized within 1.2 s versus a 2.0 s baseline, ensuring that the protective devices operate within design tolerances. Consequently, these improvements collectively reduced fault-induced DG disconnections, directly enhancing grid resilience.

This methodology effectively elevates voltage levels at all buses, thereby enhancing the system's short-circuit ratio. Validation on modified IEEE 9, 14 and 39 bus test systems via MATLAB simulations confirms that the proposed approach achieves rapid convergence and significantly improves bus voltages, resulting in enhanced system stability. In summary, this method provides an effective solution for optimizing the configuration of compensation devices.

6. Conclusions

This study addresses voltage stability challenges in power grids with large-scale distributed generation integration by proposing an optimal reactive power compensation configuration method. The approach employs short-circuit ratio criteria to identify voltage-weak nodes and utilizes the average electrical distance metric to determine optimal compensation locations. Validation through MATLAB simulations confirms the efficacy of the proposed configuration scheme. Case studies using modified IEEE 9, 14 and 39 bus test systems demonstrate effective resolution of under-/over-voltage compensation configuration problems. Following severe grid faults, this method enhances distributed generation fault ride-through capability, ensuring the secure and stable operation of highly integrated power systems. Key quantitative findings demonstrate significant improvements: minimum fault voltage increased by 0.05–0.08 p.u. across test systems, and voltage recovery time reduced by 0.15–0.8 s. These enhancements were achieved through three core innovations: an SCR < 2.0 threshold for precise weak node identification, an average electrical distance metric optimizing placement efficacy, and chance-constrained programming integrating disconnection limits.

Future research will extend this methodology to ultra-large-scale DG integration in multi-area hybrid AC/DC grids, develop real-time adaptive compensation strategies for renewable intermittency and optimize cost–stability tradeoffs with energy storage systems. These advancements will provide comprehensive solutions for modern grid stability while bridging theoretical frameworks and practical implementations. The integration of artificial intelligence algorithms and real-time optimization techniques will develop dynamic reactive compensation strategies to address intermittency and volatility challenges in renewable generation. Cost–stability tradeoff analysis will further optimize equipment configuration economics. Synergistic optimization with energy storage systems and demand response technologies will explore multi-energy coordination approaches, providing theoretical and practical support for modern grid stability. These advancements will offer comprehensive solutions for increasingly complex grid operating environments while enhancing practical applicability.

Author Contributions: Conceptualization, T.N.; Methodology, N.F., J.Y., Y.F. and Y.L.; Software, J.Y.; Validation, N.F. and J.Y.; Formal analysis, N.F.; Data curation, Y.Z.; Writing—original draft, T.N. and J.Y.; Writing—review & editing, T.N. and J.Y.; Supervision, T.N. All authors have read and agreed to the published version of the manuscript.

Funding: This research was funded by State Grid Corporation of China Technology Project (Research on optimization and evaluation technology of AVC control strategy of urban power grid under the trend of power electronics), grant number 520940230004.

Data Availability Statement: The original contributions presented in this study are included in the article. Further inquiries can be directed to the corresponding author.

Conflicts of Interest: Author Nan Feng, Jun Yan, Yufan Zhang, Yuyao Feng was employed by the company Electric Power Research Institute, State Grid Shanghai Municipal Electric Power Company. The remaining authors declare that the research was conducted in the absence of any commercial or financial relationships that could be construed as a potential conflict of interest.

References

1. Shyamal, P.; Krishna, M.; Sukumar, K. Distributed control of distributed energy resources in active power distribution system for local power balance with optimal spectralclustering. *IEEE Trans. Power Syst.* **2022**, *58*, 5395–5408. [CrossRef]
2. Zhang, C.; Dou, X.; Wang, L.; Dong, Y.; Ji, Y. Distributed cooperative voltage control for grid-following and grid-forming DGs in islanded microgrids. *IEEE Trans. Power Syst.* **2022**, *38*, 589–602. [CrossRef]
3. Wang, Y.C.; Zhang, S.; Lin, Z.Z.; Jiang, C.W.; Tang, L.; Wen, F.S. Market mechanisms and implementation methodsfor distributed sources and loads participating in ancillary services. *Autom. Electr. Power Syst.* **2023**, *47*, 3–16. [CrossRef]
4. Hao, W.; Meng, Z.; Zhang, Y.; Xie, B.; Peng, P.; Wei, J. Carrying capacity evaluation of multipledistributed power supply access to the distribution network with the background of a new power system. *Power Syst. Prot. Control* **2023**, *51*, 23–33. [CrossRef]
5. Zhang, S.; Gu, W.; Zhang, X.; Chung, C.Y.; Yu, R.; Lu, S.; Palma-Behnke, R. Analysis for integrated energy system: Benchmarking methods and implementation. *Energy Internet* **2024**, *1*, 63–80. [CrossRef]
6. Fan, Y.; Chen, N.; Zhao, Y.; Ding, X.; Zhang, R.; Zhang, X. Review of methodology and best practice of power system restoration plan. *Energy Internet* **2024**, *1*, 123–140. [CrossRef]
7. Safari, Z.; Javareshk, S.M.A.N.; Pourbagheri, M.; Niaemanesh, M.; Pakseresht, M. Congestion Management in Distribution Network: An Exploration of Distributed Generation and Demand Response Programs by Using the MOPSO Algorithm. In Proceedings of the 2023 27th International Electrical Power Distribution Networks Conference (EPDC), Mashhad, Iran, 12–15 June 2023; pp. 173–177. [CrossRef]
8. Bayati, N.; Savaghebi, M. A Transient Component-Based Technique for Fault Detection in Distributed Generation Systems. In Proceedings of the 2022 IEEE 13th International Symposium on Power Electronics for Distributed Generation Systems (PEDG), Kiel, Germany, 26–29 June 2022; pp. 1–5. [CrossRef]
9. Yuan, L.; Sun, Y.; Liu, Z.; Shao, C.; Liu, B. Influence and Optimization of Low-voltage Distributed Photovoltaic Reactive Power in Active Distribution Network Based on the Power Flow Reverse Point. *Shandong Electr. Power* **2023**, *50*, 11–19+41. [CrossRef]
10. Li, S.; Qiao, Y.; Xu, M.; Wu, L.; Lu, Z.; Xian, W. Hierarchical multi-objective safety margin optimization of renewable energy island collecting delivery system by VSC-HVDC. *Power Syst. Technol.* **2020**, *44*, 4513–4520. [CrossRef]
11. Xue, L.; Niu, T.; Fang, S.; Chen, J. Master-Slave Cooperative Dynamic Reactive Power Optimization Method Considering Transient Voltage Security of High Proportion of Wind Power. *Autom. Electr. Power Syst.* **2023**, *47*, 57–66. [CrossRef]
12. Hong, L.; Wu, M.; Wang, Y.; Shahidehpour, M.; Chen, Z.; Yan, Z. MADRL-Based DSO-Customer Coordinated Bi-Level Volt/VAR Optimization Method for Power Distribution Networks. *IEEE Trans. Sustain. Energy* **2024**, *15*, 1834–1846. [CrossRef]
13. Wang, Y.; Zhu, J.; Li, Y.; Hu, J.; Ma, S.; Wang, T. Wang, Study on AC Transient Overvoltage Suppression of LCC-HVDC Sending End System Based on DC Current Control Optimization. In Proceedings of the 2023 8th Asia Conference on Power and Electrical Engineering (ACPEE), Tianjin, China, 14–16 April 2023; pp. 2419–2424. [CrossRef]
14. Yin, C.; Li, F. Analytical expression on transient overvoltage peak value of converter buscaused by DC faults. *IEEE Trans. Power Syst.* **2021**, *36*, 2741–2744. [CrossRef]
15. Ibrahim, T.M.S.; De Rubira, T.T.; Del Rosso, A.; Patel, M.; Guggilam, S.; Mohamed, A.A. Alternating Optimization Approach for Voltage-Secure Multi-Period Optimal Reactive Power Dispatch. *IEEE Trans. Power Syst.* **2022**, *37*, 3805–3816. [CrossRef]
16. Zhu, K.; Li, L.; Xu, Y.; Zhang, T.; Zhou, L. Multi-Connection Based Scalable Video Streaming in UDNs: A Multi-Agent Multi-Armed Bandit Approach. *IEEE Trans. Wirel. Commun.* **2022**, *21*, 1156–1169. [CrossRef]
17. Wu, D. Research on New Energy Development Planning Technology. In Proceedings of the 2024 3rd Asian Conference on Frontiers of Power and Energy (ACFPE), Chengdu, China, 25–27 October 2024; pp. 638–642. [CrossRef]
18. Zhang, Y.; Yin, C.; Li, F.; Han, L.; Liu, J.; Shi, Y. A simultaneous commutation failure assessment method considering reactive powerand voltage characteristics in multi-infeed HVDC systems. *Power Syst. Prot. Control* **2024**, *52*, 170–187. [CrossRef]
19. Zhang, Z.; Wang, W.; Yu, X.; Zhou, Y.; Zhang, W. Research on optimization method of new energy grid-connected output of the receiving power grid based on short-circuit ratio constraint. *Renew. Energy Resour.* **2023**, *41*, 1658–1664. [CrossRef]
20. Huang, Q.; Cao, S.; Wu, Y.; Lin, X.; Wei, F.; Yang, D.; Cui, T. A New Multi-Infeed Short Circuit Ratio Index Taking into Account the Amplitude and Phase Characteristics of New Energy. *Proc. CSEE* **2024**, *44*, 5960–5973. [CrossRef]
21. Dong, X.; Li, G.; Qiao, R.; Liu, S.; Kan, C. Urban Distribution Network Dynamic Reactive Power Optimization Considering Electrical Vehicle Station. *Shandong Electr. Power* **2024**, *51*, 1–9. [CrossRef]

22. *IEEE Std 1547-2018*; IEEE Standard for Interconnection and Interoperability of Distributed Energy Resources with Associated Electric Power Systems Interfaces. IEEE: Piscataway, NJ, USA, 2018; pp. 1–138. [CrossRef]
23. Rayati, M.; Bozorg, M.; Cherkaou, R.; Carpita, M. Distributionally Robust Chance Constrained Optimization for Providing Flexibility in an Active Distribution Network. *IEEE Trans. Smart Grid* **2022**, *13*, 2920–2934. [CrossRef]

Disclaimer/Publisher's Note: The statements, opinions and data contained in all publications are solely those of the individual author(s) and contributor(s) and not of MDPI and/or the editor(s). MDPI and/or the editor(s) disclaim responsibility for any injury to people or property resulting from any ideas, methods, instructions or products referred to in the content.